9

# Acceleration Visualization Marker Using Moiré Fringe for Remote Sensing

Takeshi Takakai
*Hiroshima University*
*Japan*

## 1. Introduction

Advances in metrology contribute to various fields, and many sensors are developed as a result, such as high-performance devices, compact and lightweight devices, and low-cost devices, depending on the specific application environment. The sensors used in the recent years to measure physical quantities commonly feature electrical elements, and when such sensors are attached to measurement points, it is necessary to supply electrical power at these points. This implies that external power must be supplied via wiring, or, that an internal electrical power source must be fitted into the sensor. Furthermore, wired or wireless methods are needed to transmit the measurement data from the sensor.

In some environments, this can be a limiting factor for the applicability of measurements. To solve this problem, measurement techniques that do not require electrical power to be supplied to measurement points have been developed, which utilize optical elements or ultrasound, for example. In an earlier paper, we proposed a mechanism that makes the use of moiré fringes to visualize a physical force without any need for an electrical power supply at the measurement points. We also demonstrated typical applications of this technique by fitting the mechanism to a robot gripper (Takaki, 2008) and an endoscopic surgical instrument (Takaki, 2010a).

In addition, a large number of research has been carried out on the maintenance and management of large structures such as industrial plants, buildings, or bridges, by measuring their physical behavior. In particular, there have been many studies on vibrational phenomena (Umemoto, 2010) (Yun, 2010) (Kim, 2010). However, providing wiring for all the sensors in such large structures is no easy matter. We therefore propose the use of markers that utilize moiré fringes to enable acceleration to be visualized and displayed, without the need for an electrical power supply at the measurement points. In this manner, it is possible to measure acceleration remotely, without any wiring, by capturing images of the markers with a camera.

There have been previous studies on measuring displacement by means of moiré fringes (Kobayashi, 1987) (Reid, 1984) (Basehore, 1981) (Meadows, 1970) (Takasaki, 1970). Although these techniques have the advantage of not requiring a direct supply of electrical power at the measurement points, they require the use of lasers or special light sources to enable the projection of stripe patterns in order to generate the moiré fringes. The technique proposed in the present paper is different in that it does not require any special light source, but instead utilizes ambient light.

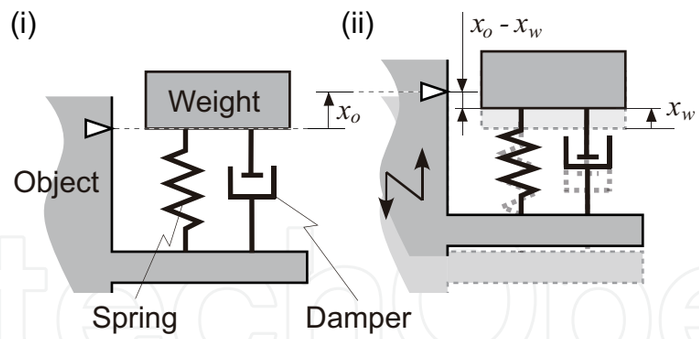


Fig. 1. Seismic system

In our proposed method, moiré fringes are generated by superimposing two glass plates, printed with parallel line gratings. Although a similar method was previously suggested for measuring displacement (Masanao, 1986), it has no provision for measuring acceleration or for the remote acquisition of data using a camera.

In the present study, we propose acceleration visualization markers (Takaki, 2010b) that enable the display of moiré fringes corresponding to the magnitude of the acceleration, and we demonstrate a method for acquiring acceleration data by means of the captured images of these markers . Chapter 2 of this report describes the principle by which the magnitude of the acceleration can be measured using moiré fringes. Chapter 3 describes the method for acquiring one-axis acceleration data using captured images of the markers, and Chapter 4 describes the method of upgrading the marker to an x- and y-axis acceleration visualization markers. Chapter 5 describes the developed markers, created using selected materials with careful attention paid to damping characteristics, and explains the mechanical characteristics of the markers. It is shown how acceleration data can be acquired using a high-speed video camera. Chapter 6 concludes this study.

## 2. Principle

### 2.1 Seismic system and acceleration

It is well known that acceleration can be measured using the seismic system (Holman, 2001), which consists of a spring, a damper, and a weight, as shown in Fig. 1 (i). Let us assume that a measurement object is under acceleration, as shown in Fig. 1 (ii), and that it moves by a displacement $x_o$. The displacement of the weight $x_w$ is caused by the influence of the acceleration. We discuss the method of calculating the acceleration of the object $\ddot{x}_o$ from the relative displacement $x_o - x_w$. Let $m$, $b$, and $k$ be the mass of the weight, viscosity of the damper, and spring constant of the spring, respectively, and these are constant. The sum of the forces acting on the weight is then

$$m\ddot{x}_w + b(\dot{x}_w - \dot{x}_o) + k(x_w - x_o) = 0, \tag{1}$$

where $\ddot{x}_w$, $\dot{x}_w$ and $\dot{x}_o$ are

$$\ddot{x}_w = \frac{d^2x_w}{dt^2}, \qquad \dot{x}_w = \frac{dx_w}{dt} \qquad \text{and} \qquad \dot{x}_o = \frac{dx_o}{dt}. \tag{2}$$

We consider the initial conditions as $x_w(0) = 0$, $\dot{x}_w(0) = 0$, and $x_o(0) = 0$. We then obtain the Laplace transform equation as follows:

$$ms^2 X_w(s) + bsX_w(s) + kX_w(s) = bsX_o(s) + kX_o(s). \tag{3}$$

Thus, $X_w(s)/X_o(s)$ is

$$\frac{X_w(s)}{X_o(s)} = \frac{bs + k}{ms^2 + bs + k}. \tag{4}$$

The transfer function of the seismic system with input $x_o - x_w$ and output $\ddot{x}_o$ is written as

$$\begin{aligned} G(s) = \mathcal{L}\left(\frac{x_w - x_o}{\ddot{x}_o}\right) &= \frac{X_w(s) - X_o(s)}{s^2 X_o(s)} \\ &= \frac{1}{s^2}\left(\frac{X_w(s)}{X_o(s)} - 1\right) \\ &= \frac{-1}{s^2 + 2\zeta\omega_n s + \omega_n^2}, \end{aligned} \tag{5}$$

where $\zeta$ is the dimensionless damping ratio and $\omega_n$ is the natural angular frequency of the system. $\zeta$ and $\omega_n$ are given by

$$\zeta = \frac{b}{2\sqrt{mk}} \quad \text{and} \quad \omega_n = \sqrt{\frac{k}{m}} \tag{6}$$

The transfer function of a system $G(s)$ can be described in the frequency domain as

$$G(j\omega) = \frac{-(1/\omega_n)^2}{1 - (\omega/\omega_n)^2 + 2\zeta(\omega/\omega_n)j} \tag{7}$$

The magnitude $|G(j\omega)|$ $(= |(x_w - x_o)/\ddot{x}_o|)$ and the phase angle $\phi$ are respectively written as

$$|G(j\omega)| = \frac{(1/\omega_n)^2}{\sqrt{\left(1 - (\omega/\omega_n)^2\right)^2 + \left(2\zeta\,(\omega/\omega_n)^2\right)^2}}$$

and

$$\phi = -\tan^{-1}\frac{2\zeta(\omega/\omega_n)}{1 - (\omega/\omega_n)^2} - \pi \tag{8}$$

When $\omega \ll \omega_n$, as shown in Fig. 2, $|G(j\omega)|$ and $\phi$ are approximately given by

$$|G(j\omega)| = \left|\frac{x_w - x_o}{\ddot{x}_o}\right| \simeq \frac{1}{\omega_n^2} \quad \text{and} \quad \phi \simeq -\pi \tag{9}$$

Therefore, the relationship between the relative displacement $x_w - x_o$ and the acceleration $\ddot{x}_o$ can be written as

$$\ddot{x}_o \simeq \omega_n^2(x_o - x_w). \tag{10}$$

According to this equation, the natural angular frequency $\omega_n$ can be obtained from constant values of the mass of the weight $m$ and spring constant $k$, as we can see by Eq. 6; therefore, $\omega_n^2$ is a constant. If the relative displacement $x_o - x_w$ is magnified sufficiently, the acceleration $\ddot{x}_o$ also becomes perceivable. However, in general, the relative displacement $x_o - x_w$ is too small to observe. Therefore, it is necessary to use a technology that can magnify the relative displacement $x_o - x_w$. We have focused on the use of a moiré fringe to magnify the relative displacement in this case.

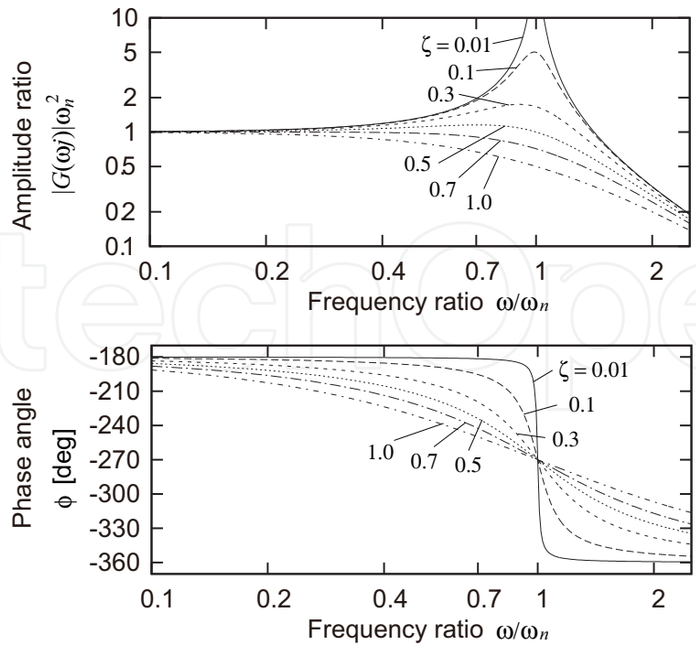


Fig. 2. Frequency response of the seismic system

### 2.2 Moiré fringe

Let us understand the concept of a moiré fringe (Kobayashi, 1987). As shown in Fig. 3 (i), line gratings 1 and 2 have the same pitch $p_g$ and line grating 2 is inclined at a small angle $\varphi$ and superimposed on line grating 1; a fringe known as the moiré fringe appears at a large pitch $p_m$ $(> p_g)$. The pitch $p_m$ is larger than the pitch $p_g$ of line gratings 1 and 2. The relationship between the pitches is given by

$$p_m = \frac{1}{2\sin\frac{\varphi}{2}}\ p_g. \tag{11}$$

As shown in Fig. 3 (ii), when line grating 1 is moved in the direction $(x)$ at pitch $p_g$, the moiré fringe moves in the direction $(X)$ at pitch $p_m$. Therefore, the displacement can be displayed visually at a magnification of $1/2\sin(\varphi/2)$. This magnification is defined as $M$. When the relative displacement of the line gratings is $x_o - x_w$, the displacement of the moiré fringe can be described by the following equation:

$$x_m = M(x_o - x_w). \tag{12}$$

### 2.3 Structure of the acceleration visualization marker

To obtain a constant magnification $M$ using moiré fringes, as described in Section 2.2, even if a relative displacement $x_o - x_w$ occurs, the angle $\varphi$ must be maintained as a constant. To satisfy this requirement, two elastic plates of the same shape are used, as shown in Fig. 4 (i). This structure permits a relative displacement $x_o - x_w$ without any change in the angle $\varphi$, as shown in Fig. 4 (ii). Moreover, the elasticity and the damping capacity of the elastic plates function as the spring and the damper of the seismic system, respectively. If a weight is installed in this structure, it becomes a seismic system, and the acceleration $\ddot{x}_o$ can be calculated from the relative displacement $x_o - x_w$.

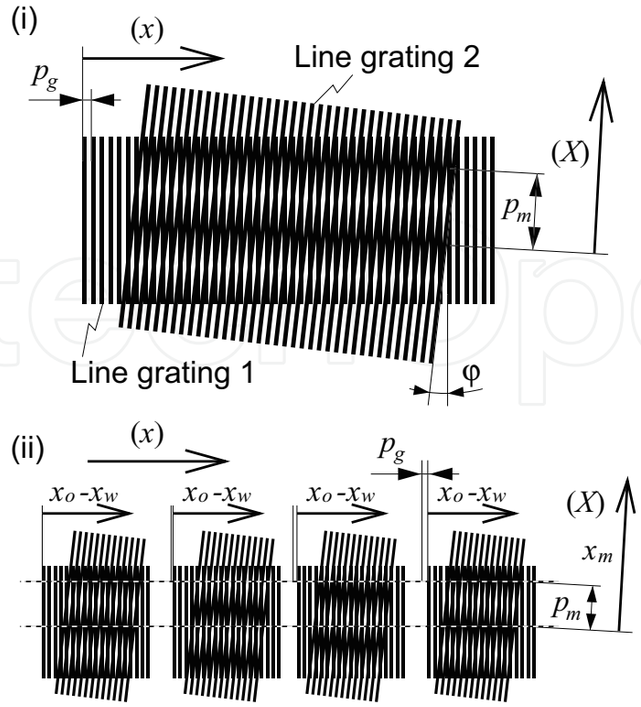


Fig. 3. A moiré fringe

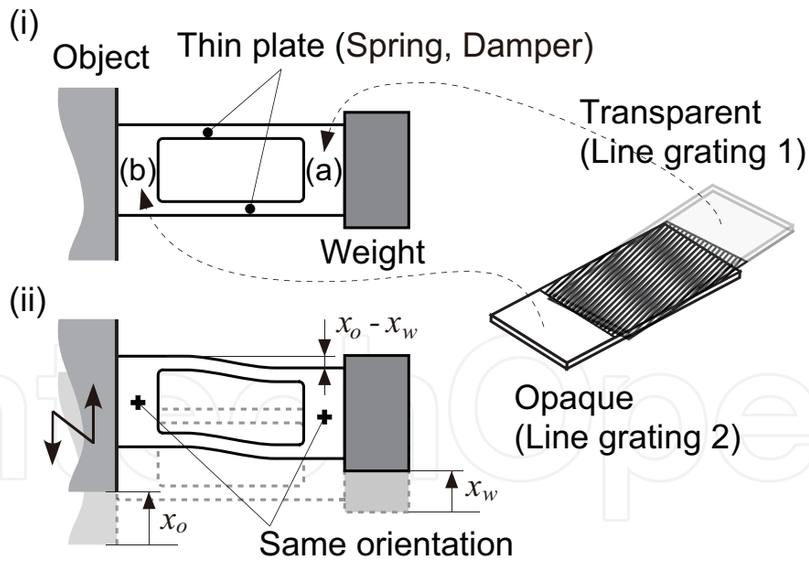


Fig. 4. Structure of the acceleration visualization marker

Line gratings 1 and 2 are respectively printed on transparent and opaque glass plates and fixed at locations (a) and (b) as shown in Fig. 4. The relative displacement $x_o - x_w$ produced by the acceleration $\ddot{x}_o$ is displayed by the moiré fringe at magnification $M$. Therefore, the magnitude of the acceleration $\ddot{x}_o$ can be confirmed visually. These acceleration visualization elements combine to form the acceleration visualization marker.

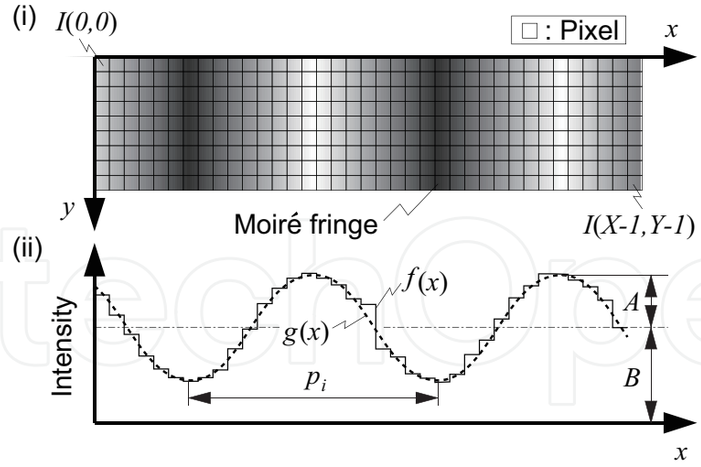


Fig. 5. Intensity of a moiré fringe and a fitted curve

## 3. Method of extracting acceleration value by image processing

### 3.1 Fitted sine curve

The image of a moiré fringe is trimmed from an original image taken by a camera, and the $x$- and $y$-axes are defined as shown in Fig. 5 (i). The size of the trimmed image is $(X, Y)$, and the brightness value of the pixel at $(x, y)$ is defined as $I(x, y)$. $f(x)$ is the average of the brightness value along the y-axis. $f(x)$ can be written as

$$f(x) = \frac{\sum_{k=0}^{Y-1} I(x,k)}{Y} \tag{13}$$

$g(x)$ is a fitted sine curve of $f(x)$. $g(x)$ can be written as follows:

$$g(x) = A\sin(\frac{2\pi}{p_i}x + \theta) + B \tag{14}$$

Figure 5 (ii) shows the difference between $f(x)$ and $g(x)$ in a example case. $p_i$, $A$, $B$, and $\theta$ are the pitch, amplitude of the brightness value, offset of the brightness value, and phase of the moiré fringe in the trimmed image, respectively. $p_i$ can be obtained from an autocorrelation analysis of $f(x)$, and $A$, $B$, and $\theta$ can be obtained using the least square method.

### 3.2 Phase of fitted sine curve and displacement of moiré fringe

Figure 6 (i) shows the image of a moiré fringe when no acceleration is applied to the acceleration visualization marker. The brightness value of this moiré fringe is fitted to $g(x)$, and the phase in this state is assumed to be $\theta_0$, as indicated by (a) in Fig. 6 (iii). When acceleration is applied to the marker, a relative displacement of $x_o - x_w$ occurs, and the moiré fringe moves by $x_m$, which can be calculated from Eq. (12). In the image, when a unit length corresponds to $l$ pixels, the moiré fringe moves by $lx_m$, as shown in Fig. 6 (ii). When the phase $\theta$ shifts by $\Delta\theta$, as indicated by (b) in Fig. 6 (iii), the relationship between these two terms is given by

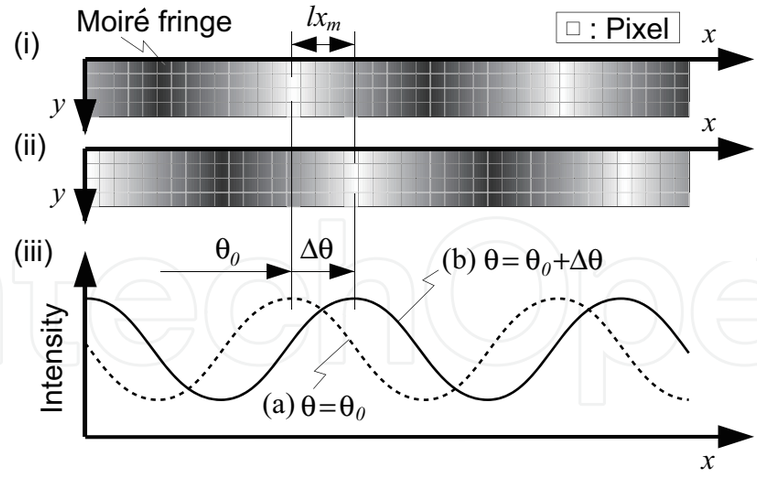


Fig. 6. Phase of a moiré fringe

$$lx_m = \frac{p_i}{2\pi}\Delta\theta \tag{15}$$

From Eqs. (10), (12), and (15), the acceleration $\ddot{x}_o$ is given by

$$\ddot{x}_o \simeq \frac{\omega_n^2 p_i}{2\pi l M}\Delta\theta \tag{16}$$

Here, phase $\Delta\theta$ can take the value $\Delta\theta + 2\pi n$ ($n$ is an integer) because a sine curve is a periodic function. Therefore, it is necessary to obtain the value of $n$. Let $\Delta\theta_n$ and $\Delta\theta_{n-1}$ be the phase $\Delta\theta$ calculated from current image data and one frame of previous image data, respectively. When the frame rate of the video camera is high, the difference between $\Delta\theta_n$ and $\Delta\theta_{n-1}$ takes a small value, and it can be assumed that

$$|\Delta\theta_n - \Delta\theta_{n-1}| < \pi. \tag{17}$$

When $\Delta\theta_{n-1}$ is known, the value of $n$ can be known because the range of $\Delta\theta_n$ is limited.

## 4. $x$- and $y$-axis acceleration visualization marker

The previous chapter described the one-axis maker. This chapter describes a method of upgrading the marker to an $x$- and $y$-axis acceleration marker. Fig. 7(i) shows a moiré fringe having the same configuration as that shown in Fig. 3. When line gratings 1 and 2 in Fig. 7(i) are rotated by 90°, the moiré fringe is also rotated by 90°, as shown in Fig. 7(ii). This moiré fringe moves in the direction (Y) when line grating 1′ is moved in the direction (y). Fig. 7(iii) shows a square grating which can be obtained by combining the line gratings shown in Fig. 7 (i) and Fig. 7 (ii), and a square-shaped moiré fringe is observed. When square grating 1 is moved in the directions (x) and (y), the square-shaped moiré fringe moves in the directions (X) and (Y). Therefore, even a slight displacement along the $x$- and $y$-axes can be magnified and displayed visually.

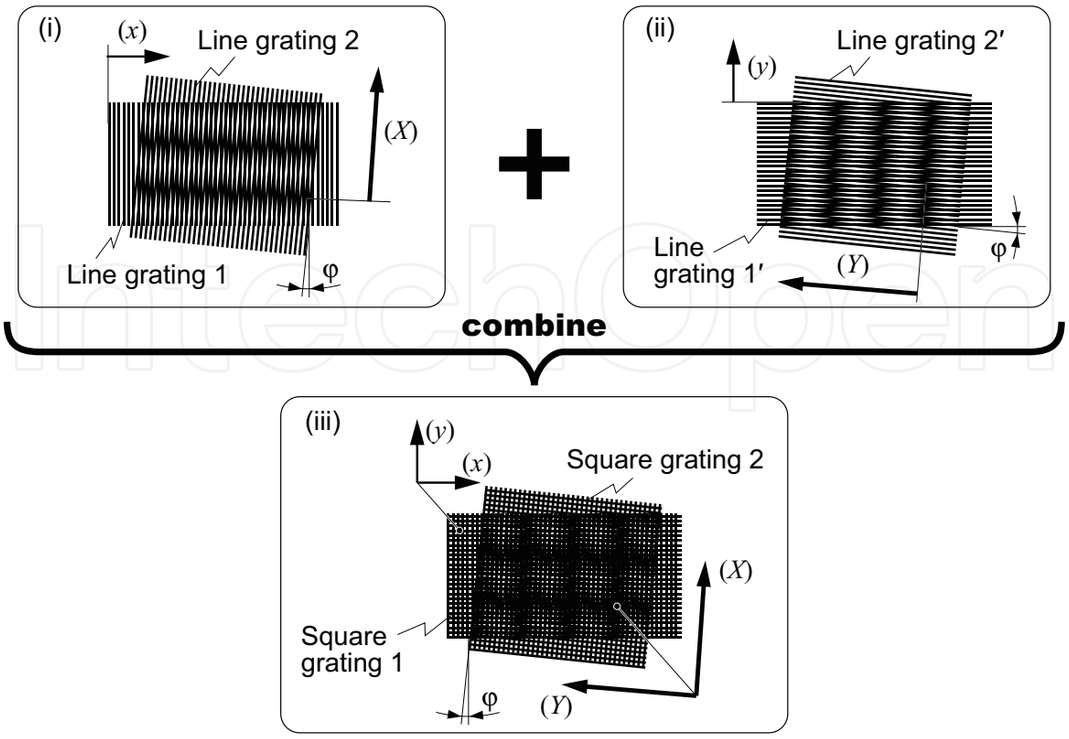


Fig. 7. Combination of two moiré fringes

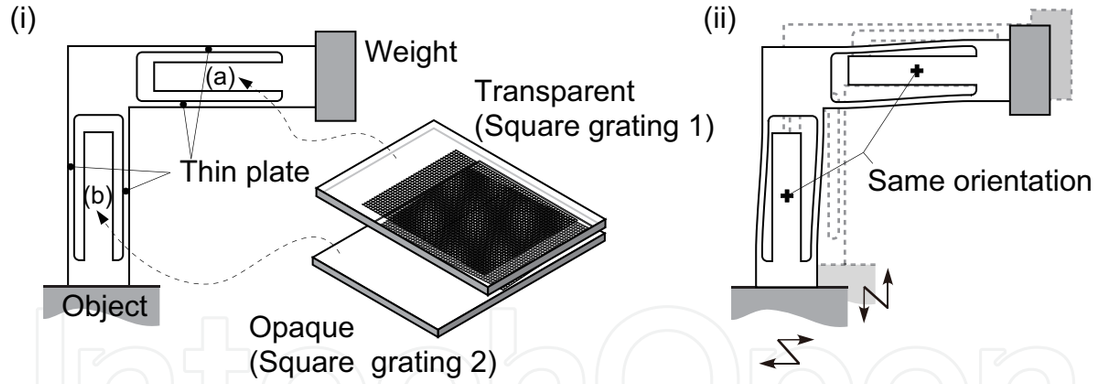


Fig. 8. Structure of the $x$- and $y$-axis acceleration visualization marker

For the same reasons as those described in Section 2.3, the angle $\varphi$ must be maintained as a constant. To satisfy this requirement, two horizontal elastic plates and two vertical elastic plates are used, as shown in Fig. 8(i). This structure permits $x$- and $y$-axis displacement without any change in the angle $\varphi$, as shown in Fig. 8(ii). Line gratings 1 and 2 are respectively printed on opaque and transparent glass plates and fixed at locations (a) and (b) shown in Fig. 8. The $x$- and $y$-axis relative displacements produced by $x$- and $y$-axis acceleration components are displayed by the moiré fringe at magnification $M$. If a weight is installed in this structure, it becomes a seismic system, and the $x$- and $y$-axis acceleration values can be calculated using same algorithm as that described in Section 3.

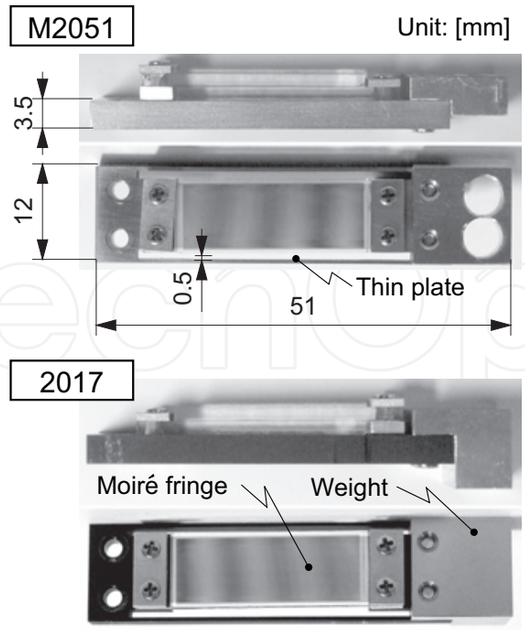


Fig. 9. Developed acceleration visualization marker

## 5. Experiment

### 5.1 Developed 1-axis acceleration visualization marker

The damping characteristic of the elastic plates influences the performance of the acceleration visualization marker. We selected two materials for the elastic plates: M2052 and 2017. M2052 includes manganese (73%), copper (20%), nickel (5%), and iron (2%), and it has a high damping capacity (Kawahara, 1993a) (Kawahara, 1993b). 2017 is an aluminum base alloy and its damping capacity is low. Figure 9 shows the developed 1-axis acceleration visualization marker, and, as shown, the shape of the elastic plates is the same.

The pitch of the line grating $p_g$ is 0.02 mm, and its line thickness is 0.01 mm. The pitch of the moiré fringe $p_m$ of the developed marker by using M2052 is 6.1 mm, and the relative displacement $x_o - x_w$ can be displayed visually at a magnification $M$ of 303. The total mass is 11.7 g. The values of $p_m$, $M$, and the total mass in the case where 2017 is used are 5.5 mm, 277, and 13.0 g, respectively.

For a comparison of the accuracies of the acceleration values obtained using the marker and calculated using the algorithm described in Section 2.1, the same natural angular frequency $\omega_n$ needs to be maintained. To adjust the natural angular frequency $\omega_n$, we machined the weight and adjusted its mass. Therefore, the shape of the weight became different. Details related to the natural angular frequency $\omega_n$ are described in Section 5.5.

### 5.2 Natural angle frequency and damping capacity of the 1-axis marker

To examine the mechanical characteristics of the developed 1-axis acceleration visualization marker, the marker was freely vibrated and the displacement of the weight was measured with a laser displacement sensor (KEYENCE, LK-G30). The experimental result is shown in Fig. 10. The natural angular frequency $\omega_n$ of the markers made M2052 is 409 rad/s (=65.1

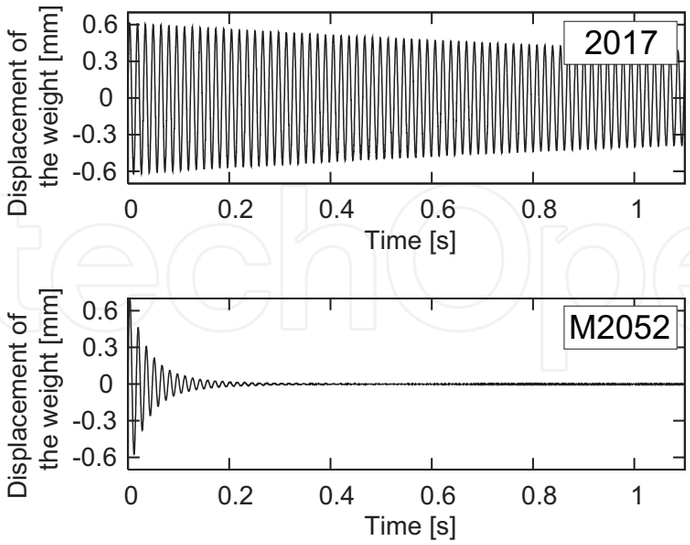


Fig. 10. Damped free vibration

Hz), and the damping ratio $\zeta$ is 0.0473. Values of $\omega_n$ and $\zeta$ obtained when marker are made using 2017 are 406 rad/s (=64.6 Hz) and 0.0011, respectively. The vibration of the composed marker of M2052 attenuates faster than that composed of 2017.

### 5.3 Acceleration measurement using the 1-axis marker

Using image processing, the proposed marker was verified to be able to provide an accurate value of acceleration. Figure 11 shows the experimental setup. The developed 1-axis markers made using M2052 and 2017 are attached to a vibration exciter. For comparison, a conventional 3-axis acceleration sensor (Freescale Semicondutor, MMA7260Q) is also attached to the vibration exciter. A high-speed camera (Photron, FASTCAM-1024PCI) takes images of the marker from a distance of 470 mm at 2000 fps. A distance of 1 mm corresponds to 6.0 pixels in the taken image, and the size of the image is 1024×512 pixels. The amplitude of the vibration exciter is measured by the laser displacement sensor. A LED is used to achieve the synchronization of the high-speed camera, the laser displacement sensor, and the acceleration sensor.

Figure 12 shows the image of a moiré fringe trimmed from the image obtained from the high-speed camera. Its size is 125×100 pixels. Figure 13 shows the average of the brightness value along the y-axis, $f(x)$, and the fitted sine curve $g(x)$. Figure 14 shows the acceleration values obtained from the markers made using M2052 and 2017 and from the acceleration sensor when the vibration exciter vibrates at 13 Hz. The amplitude of the vibration exciter is 0.58 mm.

The acceleration value obtained from the marker made using M2052 is close to that obtained from the acceleration sensor. However, the corresponding value obtained from the marker made using 2017 has an additional acceleration component at 65 Hz. The root mean square errors for the proposed method using M2052 or 2017 as materials for the marker and the 3-axis acceleration sensor are 0.24 m/s$^2$ and 1.4 m/s$^2$, respectively. Higher accuracy can be obtained from the marker made using M2052 than from that made using 2017.

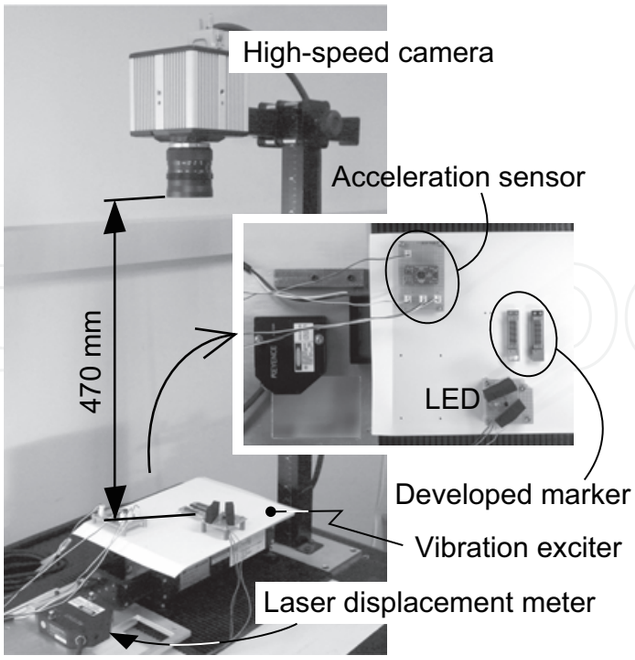


Fig. 11. Experimental setup for developed markers

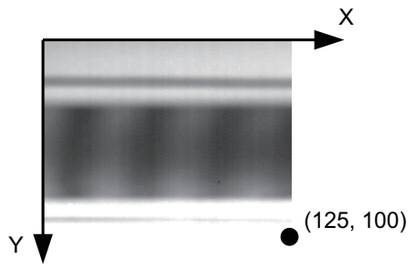


Fig. 12. Image of a moiré fringe

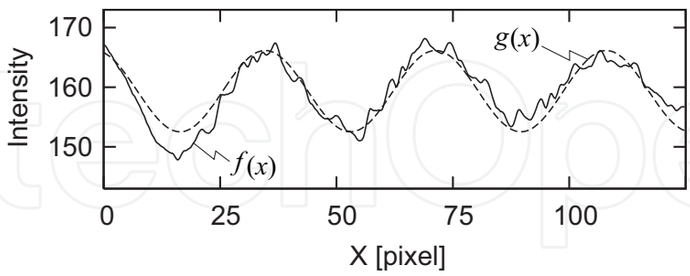


Fig. 13. Intensity of an image and a fitted curve

Figure 15 shows the power spectra of the acceleration values obtained from the acceleration sensor and the proposed markers made using M2052 and 2017. All the power spectrums have a peak at 13 Hz. This peak corresponds to the frequency of the vibration exciter. The natural angular frequencies $\omega_n$ of the two developed markers are both approximately 400 rad/s (=65 Hz). The power spectrum of the marker made using M2052 is close to that of the acceleration sensor at 65 Hz. However, the power spectrum of the marker made using 2017 has a strong sharp peak at 65 Hz. This is because it vibrates sympathetically with the slight vibration of 65

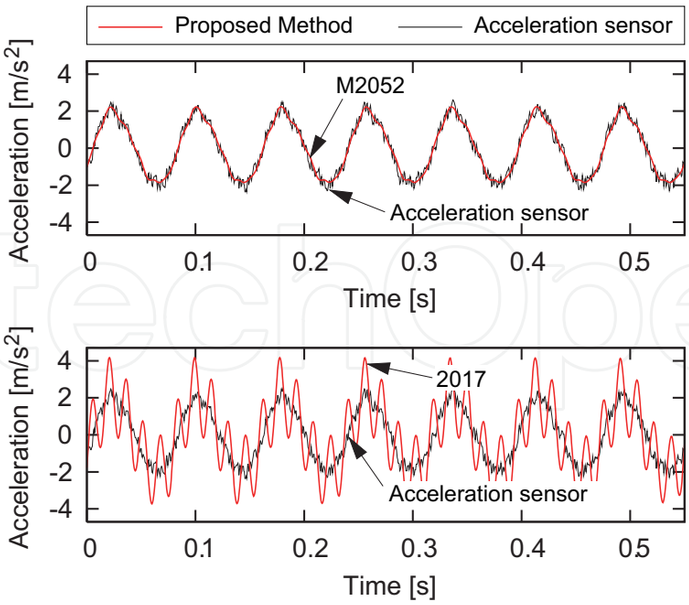


Fig. 14. Experimental result showing acceleration values

Hz included in the vibration exciter and does not attenuate because its damping ratio is small, as described in Section 5.5. Therefore, the high-damping material M2052 is more suitable for the acceleration visualization marker than the low-damping material 2017.

### 5.4 Developed $x$- and $y$-axis acceleration visualization marker

Figure 16 shows the developed $x$- and $y$-axis acceleration visualization marker. The material used for the elastic plates is M2052. The pitch of the line grating $p_g$ is 0.03 mm, and its line thickness is 0.01 mm. The pitch of the moiré fringe $p_m$ is 8.9 mm, and the relative displacement $x_o - x_w$ can be displayed visually at a magnification of 298. The total mass is 33 g.

### 5.5 Natural angle frequency and damping capacity of the $x$- and $y$-axis acceleration visualization marker

To obtain the natural angular frequency $\omega_n$ and the damping ratio $\zeta$ of the developed $x$- and $y$-axis acceleration visualization marker, the marker was freely vibrated and the displacement of the weight was measured with the laser displacement sensor. The experimental results are shown in Fig. 17. The natural angular frequencies $\omega_n$ for the $x$- and $y$-axes are 300 rad/s (=47.7 Hz) and 323 rad/s (=51.4 Hz), respectively, and the damping ratios $\zeta$ are 0.114 and 0.093, respectively.

### 5.6 Acceleration measurement using the $x$- and $y$-acceleration visualization marker

The developed $x$- and $y$-axis acceleration visualization marker could provide an accurate value of $x$- and $y$-axis acceleration, as confirmed by using image processing. Figure 18 shows the experimental setup. The developed $x$- and $y$-axis marker is attached to a vibration exciter. For comparison, the 3-axis acceleration sensor is also attached to the vibration exciter. The camera takes images of the marker from a distance of 600 mm at 2000 fps. A distance of 1 mm corresponds to 3.6 pixels in the taken image, and the size of the image is 512 $\times$ 512 pixels. The

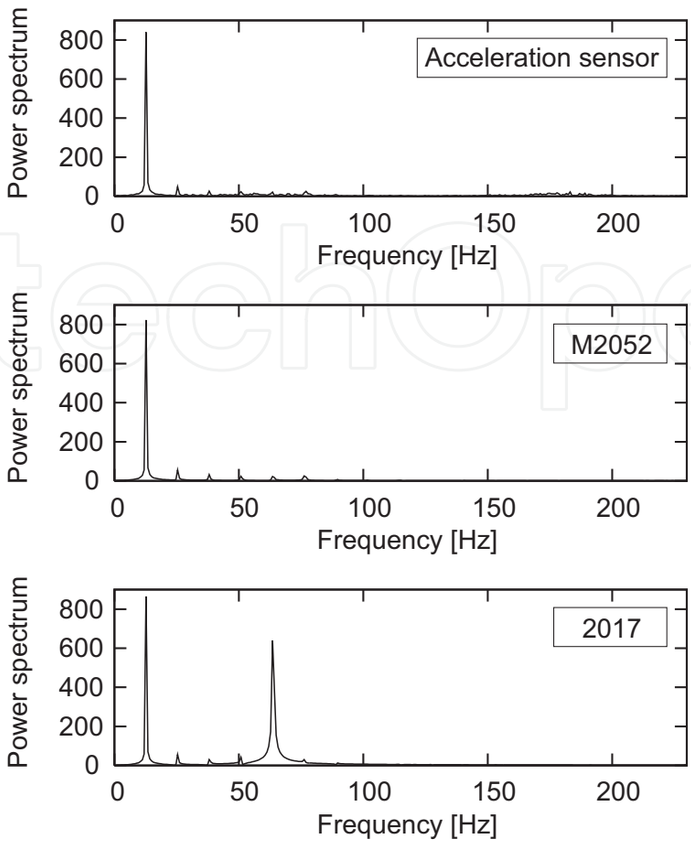


Fig. 15. Power spectra of acceleration values obtained using different devices

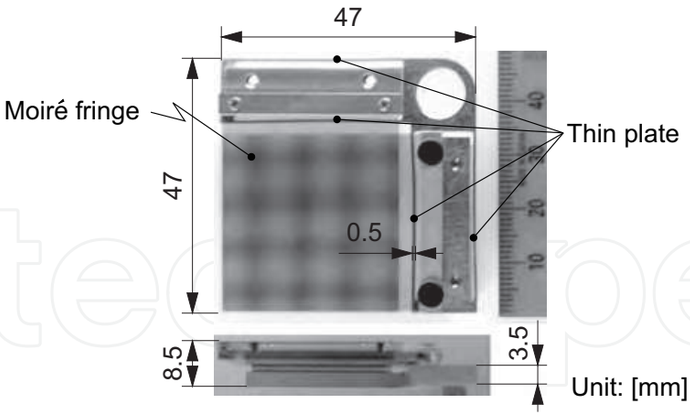


Fig. 16. Developed $x$- and $y$-axis acceleration visualization marker

amplitude of the vibration exciter is measured using the laser displacement sensor. A LED is used to obtain the synchronization of the high-speed camera, the laser displacement sensor, and the acceleration sensor.

Figure 19 shows the acceleration values obtained from the $x$- and $y$-axis markers and from the acceleration sensor when the amplitude of the vibration exciter is less than 1 mm. The acceleration value obtained from the markers is close to that obtained from the acceleration

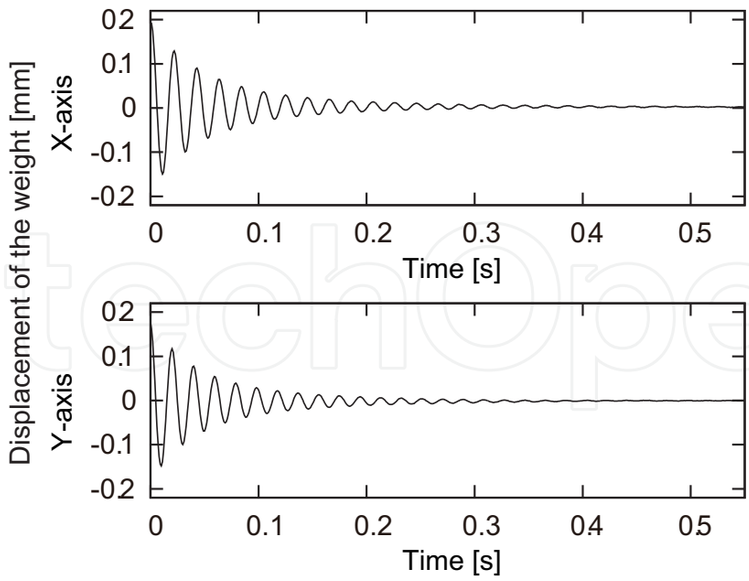


Fig. 17. Mechanical characteristic of the $x$- and $y$-axis acceleration visualization marker

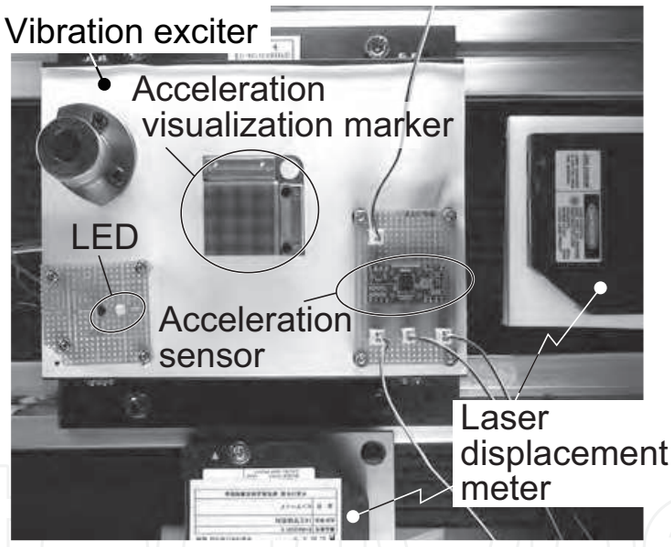


Fig. 18. Experimental setup of the $x$- and $y$-axis acceleration visualization marker

sensor. The root mean square errors for the $x$- and $y$-axis acceleration values given by the proposed method and those given by the 3-axis acceleration sensor are 0.22 $m/s^2$ and 0.23 $m/s^2$, respectively.

Figure 20 shows the power spectra of the signals shown in Fig. 19. The natural angular frequencies $\omega_n$ of the x-axis, 323 rad/s (=51.4 Hz), and y-axis, 300 rad/s (=47.7 Hz), are not observed in the power spectra for x- and y-axis acceleration values obtained using the proposed marker, and the obtained values are close to the acceleration value given by the acceleration sensor.

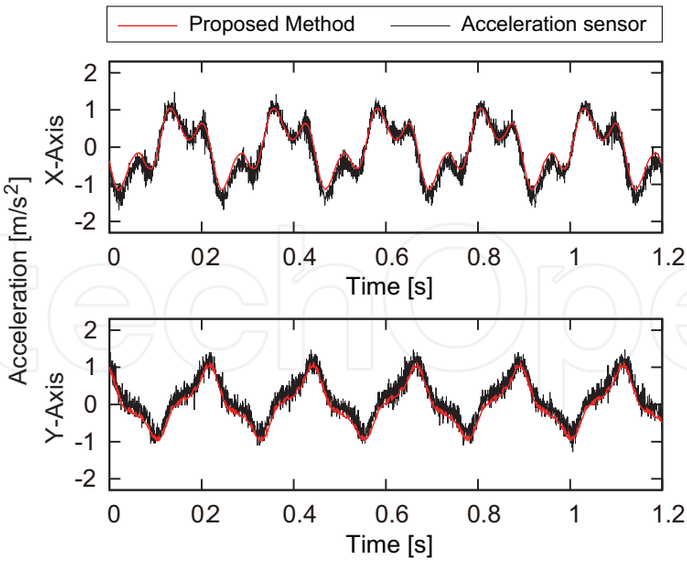


Fig. 19. Experimental result for the $x$- and $y$-axis acceleration visualization marker

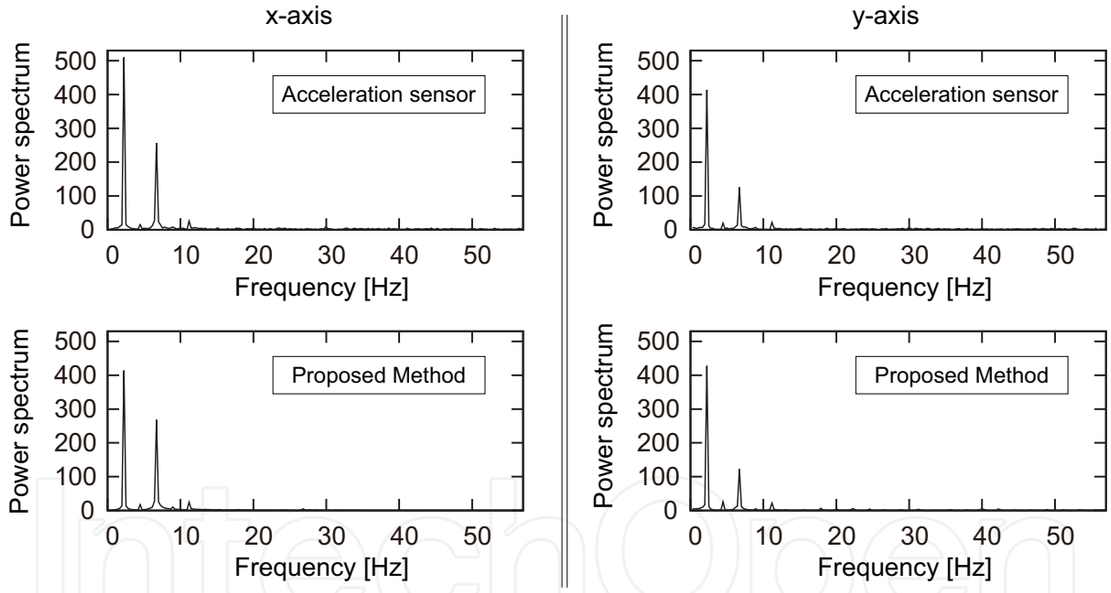


Fig. 20. Power spectra for the $x$- and $y$-axis acceleration visualization marker

## 6. Conclusion

This paper presents an acceleration visualization marker that uses a moiré fringe. It can enable the visualization of acceleration without the use of electrical elements such as amplifiers and strain gauges and can provide an accurate value of acceleration using image processing. Our future work will involve the measurement of the acceleration value from a remote place located more than 100 m away by using a telephoto lens.

## 7. References

Takaki, T.; Omasa, Y. & Ishii, I. (2008). Force Visualization Mechanism using Moiré Fringe for Robot Grippers, *Proceedings of the 28th Annual Conference of the Robotics Society of Japan*, 1K3-07, 2008. (in Japanese)

Takaki, T.; Omasa, Y.; Ishii, I.; Kawahara, T.; & Okajima, M. (2010). Force Visualization Mechanism Using a Moiré Fringe Applied to Endoscopic Surgical Instruments, *Proceedings of the 2010 IEEE International Conference on Robotics and Automation*, pp. 3648-3653, 2010.

Umemoto, S.; Fujii, M.; Miyamoto, N.; Okamoto, T.; Hara, T.; Ito, H. & Fujino, Y. (2010). Deflection measurement for bridges with frequency-shifted feedback laser, *Proceedings of the Bridge Maintenance, Safety, Management and Life-cycle Optimization*, pp. 2570-2574, 2010.

Yun, C. -B.; Soho, H.; Jung, H. J.; Spencer, B. F. & Nagayama, T. (2010). Wireless sensing technologies for bridge monitoring and assessment, *Proceedings of the Bridge Maintenance, Safety, Management and Life-cycle Optimization*, pp. 113-132, 2010.

Kim, C. W.; Kawatani, M.; Ozaki, R.; Makihata, N.; & Kano, M. (2010). Low-cost wireless sensor node for vibration monitoring of infrastructures, *Proceedings of the Bridge Maintenance, Safety, Management and Life-cycle Optimization*, pp. 780-786, 2010.

Kobayashi, A. S. (1987). *Handbook on Experimental mechanics*, Prentech-hall, ISBN 0-13-377706-5.

Reid, G. T. (1984). Moiré firnges in metrology, *Optics and Lasers in Engineering*, Vol. 5, pp. 63-93, 1984.

Basehore, M. L.; & Post, D. (1981). Moiré method for in-plane and out-of-plane displacement measurements *Applied Optics*, Vol. 21, No. 9, pp. 321-328, 1981.

Meadows, D. M.; Johnson, W. O.; & Allen, J. B. (1970). Generation of Surface Contours by Moiré Patterns, *Applied Optics*, Vol. 9, No. 4, pp. 942-947, 1970.

Takasaki, H. (1970). Moiré Topography, *Applied Optics*, Vol. 9, No. 6, pp. 1467-1472, 1970.

Takaki, T.; Omasa, Y.; & Ishii, I. (2010). Acceleration Visualization Marker using Moiré Fringe for Remote Sensing, *Transactions of the Japan Society of Mechanical Engineers, Series C*, Vol. 76, No. 770, pp. 2592-2597, 2010. (in Japanese)

Masanao, M. (1986). *Sensing Techniques of Mechanical Quantities*, Corona Publishing Co., Ltd., ISBN 4-627-61161-7. (in Japanese)

Holman, J. P. (2001). *Experimental Method for Engineers*, Thomes Casson, ISBN 0-07-366055-8.

Kawahara, K.; Sakuma, N.; & Nishizaki, Y. (1993). Effect of Third Elements on Damping Capacity of Mn-20Cu Alloy, *Journal of the Japan Institute of metals*, Vol. 57, No. 9, pp. 1089-1096, 1993. (in Japanese)

Kawahara, K.; Sakuma, N.; & Nishizaki, Y. (1993). Effect of Fourth Elements on Damping Capacity of Mn-20Cu-5Ni Alloy, *Journal of the Japan Institute of metals*, Vol. 57, No. 9, pp. 1097-1100, 1993. (in Japanese)

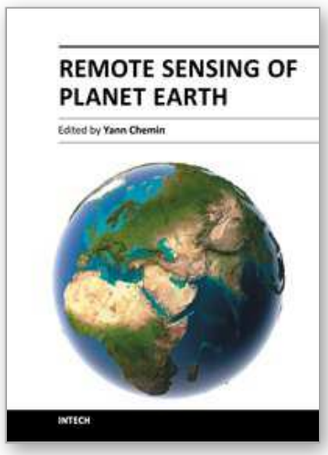


**Remote Sensing of Planet Earth**

Edited by Dr Yann Chemin

ISBN 978-953-307-919-6
Hard cover, 240 pages
**Publisher** InTech
**Published online** 27, January, 2012
**Published in print edition** January, 2012

Monitoring of water and land objects enters a revolutionary age with the rise of ubiquitous remote sensing and public access. Earth monitoring satellites permit detailed, descriptive, quantitative, holistic, standardized, global evaluation of the state of the Earth skin in a manner that our actual Earthen civilization has never been able to before. The water monitoring topics covered in this book include the remote sensing of open water bodies, wetlands and small lakes, snow depth and underwater seagrass, along with a variety of remote sensing techniques, platforms, and sensors. The Earth monitoring topics include geomorphology, land cover in arid climate, and disaster assessment after a tsunami. Finally, advanced topics of remote sensing covers atmosphere analysis with GNSS signals, earthquake visual monitoring, and fundamental analyses of laser reflectometry in the atmosphere medium.



**InTech Europe**
University Campus STeP Ri
Slavka Krautzeka 83/A
51000 Rijeka, Croatia
Phone: +385 (51) 770 447
Fax: +385 (51) 686 166
www.intechopen.com

**InTech China**
Unit 405, Office Block, Hotel Equatorial Shanghai
No.65, Yan An Road (West), Shanghai, 200040, China
中国上海市延安西路65号上海国际贵都大饭店办公楼405单元
Phone: +86-21-62489820
Fax: +86-21-62489821

IntechOpen